AIP | Journal of Applied Physics

# E cts o u i xi pr ssur o po r hisp ri g g ry od s i icrosph r s

H P g r H Sch itz r J Lutti P Borri d L g i

Cit tio : J App Phys 3 43 0 ( 0 3 ; doi: 0 063 48 447
Vi o i : http: dx doi org 0 063 48 447
Vi T o Co t ts: http: p ip org r sourc JAPIAU 3 i 4
Pu ish d y th AIP Pu ishi g LLC

# Effects of uniaxial pressure on polar whispering gallery modes in microspheres

H. P. Wagner,[1] H. Schmitzer,[2] J. Lutti,[3] P. Borri,[4] and W. Langbein[3]
[1]*Department of Physics, University of Cincinnati, Cincinnati, Ohio 45221, USA*
[2]*Department of Physics, Xavier University, Cincinnati, Ohio 45207, USA*
[3]*School of Physics and Astronomy, Cardiff University, The Parade, Cardiff CF24 3AA, United Kingdom*
[4]*School of Biosciences, Cardiff University, Museum Avenue, Cardiff CF10 3US, United Kingdom*

(Received 28 February 2013; accepted 3 June 2013; published online 24 June 2013)

We investigate the detuning of whispering gallery modes (WGMs) in solid polystyrene microspheres (PM) as a function of axisymmetric stress applied to two antipodal points of the microsphere we call poles. We specifically investigate WGMs passing close to these poles, so-called polar WGMs. The applied uniaxial pressure reduces the geometrical circumference of the PM but also increases locally the refractive index at the flattened poles. Our experiments show that the WGMs shift to higher frequencies with increasing pressure and that the magnitude of the strain-induced shift depends on the radial mode number $n$. Furthermore an energy splitting between azimuthal modes linearly increasing with the pressure is observed. A theoretical model based on a classical ray optics approach is presented which reproduces the main results of our experimental observations. © *2013 AIP Publishing LLC*. [http://dx.doi.org/10.1063/1.4811447]

## I. INTRODUCTION

Optical microsphere resonators supporting whispering gallery modes (WGM)[1] have recently attracted interest because of their potential for a range of applications.[2] The high quality factor $Q = \nu/\Gamma$, where $\nu$ is the center frequency and $\Gamma$ is the full width at half maximum (FWHM), of the WGMs of up to $10^{10}$ (Refs. 3 and 4) has given rise to studies on the lasing properties of droplets and microspheres.[5–8] In addition, the WGMs can be tuned thermally[9,10] by uniaxial stress[11–14] or by electric[15–17] or magnetic fields.[18] Various sensors based on this energy shift[12,19,20] as well as photonic receivers have been suggested.[21] The evanescent light field of the WGMs close to the sphere surface provides sensitivity to changes in the environment,[22–24] and the subsequent shift of the resonance energy has been used for single virus[25] and single bacterium detection[23] as biosensors.[26,27]

In this paper we present investigations on *polar* WGMs in solid polystyrene microspheres (PM) of about 40 $\mu$m diameter subject to polar uniaxial stress. Polar WGMs propagate across the poles of a microsphere given by the antipodal locations of the applied stress. While the resonance shift of equatorial WGMs under uniaxial pressure has been investigated both theoretically and experimentally (see Refs. 11–13) the effects of uniaxial stress on polar WGMs have not been studied so far. Our investigations are motivated by the strong deformation at the PM caps along the light path, influencing the WGM resonances and potentially providing enhanced pressure sensitivity compared to equatorial WGMs. The WGMs are characterized by the radial mode order $n$ which is defined as the number of nodes of the radial field distribution plus one, by the orbital angular quantum number $l$ and by its quantized projection $m$ onto the polar z-axis defined by the uniaxial pressure direction. The changes in the WGM frequency for different radial mode orders $n$ and mode numbers $l$, in the splitting between azimuthal modes (characterized by the projection quantum number $m$) as well as in their linewidth as a function of the applied uniaxial force, are reported in Sec. III. A theoretical description based on a one-dimensional ray-optics model will be presented in Sec. IV in order to describe the observed energy shift as well as the splitting of $m$-modes of polar WGMs in uniaxially stressed PMs.

## II. EXPERIMENTAL DETAILS

Polystyrene microspheres of 43 $\mu$m average diameter are mounted between the side walls of a homebuilt flow chamber[22,23] with controlled fluidic delivery using a syringe and two-sided optical access. The distance between the side walls has been carefully adjusted to the diameter of the PMs by an inserted Latex® film of matching thickness in order to limit the uniaxial strain in the microspheres caused by the mount. The PMs are attached to the flat surface of a high-index half-ball lens ($n = 1.826$) coated with a separation layer of Cytop®, which has a refractive index of 1.34 closely matching the surrounding liquid water. Thus its presence at the sphere poles does not alter the WGM modes significantly. The thickness of the Cytop® layer was adjusted to about 500 nm in order to facilitate the coupling of the whispering gallery modes to the evanescent field at the surface of the half-ball lens.[22] A sketch of the flow chamber and optical set-up is given in Fig. 1. For the stress dependent measurements a cantilever with a tip of a needle exerted a force normal to the thin ($\sim$150 $\mu$m) rear window of the sample chamber, which was also coated with a Cytop® layer. The magnified side view of the flow chamber schematically shows the deformed bead with excited $m$-modes in the ray-optical one-dimensional picture.

To estimate the stress on the PM, we assume that PM, window, and cantilever form a compound system of springs. The spring constant $k_s = 62.2 \pm 0.1$ N/m of the cantilever

 

was measured separately. The "effective" spring constant of the mounted thin window (microscope cover slip of 150 $\mu$m thickness and with a diameter of 23 mm) between cantilever and bead was determined to be $k_w = 30 \pm 2$ kN/m, by measuring the displacement of the window with a microscope objective when pressing with the calibrated cantilever from the rear side onto the window. The deformation of the half ball lens was neglected due to its much larger stiffness. A microscope objective and a video camera on the thin window side allowed adjusting the cantilever tip on top of one PM and counting the number of the polystyrene beads being enclosed in the flow chamber. A photograph of two beads with the cantilever close to the excited bead is shown at the bottom of Fig. 1. As all PMs were situated close to the center of the chamber, we assume that they act like parallel springs to estimate the applied uniaxial force on the PM under investigation.

The WGMs were optically excited using a tunable distributed feedback (DFB) laser emitting at a wavelength of about 770 nm, corresponding to a photon energy of about 1.6 eV. Below threshold the DFB laser provides a spectrally broad emission which we used for excitation of WGMs over a spectral range of several tens of meV. The beam is focused onto the planar interface between the high index half ball lens and the Cytop® layer, where it is totally internally reflected. The exciting beam couples to the WGMs when a PM is positioned in the evanescent field of the excited spot. The spot diameter and the excitation angle to the surface normal were adjusted to ~5 $\mu$m and ~55°, respectively, in order to optimize the coupling to the WGMs. The reflected light from the PM is dispersed by a 2-m high-resolution (~6 $\mu$eV) grating spectrometer and detected by a cooled charge-coupled-device (CCD) camera enabling the observation of coupled WGMs as sharp dips in the reflectivity spectrum. Both horizontal and vertical polarizations, which couple to the transverse magnetic (TM) and transverse electric (TE) WGMs, respectively, were used. Once the WGM frequencies were found using the spectrometer and the contrast was optimized, high resolution spectra were recorded using the DFB laser operating above threshold with a linewidth of ~16 neV (4 MHz). The emission energy was temperature tuned onto the WGM of interest (tuning range 5 meV corresponding to 1.2 THz frequency and 2.4 nm wavelength) and then scanned over a range of 350 $\mu$eV corresponding to 85 GHz and 0.17 nm, across the resonance using a triangular current modulation at about 50 Hz. In this tunable DFB detection method, the reflected TE and TM power was detected using two photodiodes, and the current difference was recorded with an oscilloscope.

## III. EXPERIMENTAL RESULTS

### A. Microspheres at low offset uniaxial stress

Figure 2 shows the TE and TM polarized reflectivity spectra of WGMs of a polystyrene microsphere. The spectra were recorded with the CCD camera using the high-resolution grating spectrometer in first order diffraction, and a calcite polarization displacer in front of the spectrometer input slit to separate the TE and TM intensities along the slit and thus on the CCD camera. To compensate for systematic spectral sensitivity, the TE polarized spectrum was divided by the TM spectrum. Mode orders $n$, mode numbers $l$ (given as subscript), and the sphere diameter have been determined by comparison of the resonance energies with calculations based on explicit asymptotic formulas for spherical PM's.[22,28] The mode number $l$ for a given mode order ($n = 1$ to 4) increases towards higher energy, having a relative separation of about $1/l$. For the investigated PM the diameter was determined to be $43.5 \pm 0.2$ $\mu$m, using a refractive index of 1.58 for polystyrene[22] and 1.33 for water at 1.585 eV photon energy.

Figure 3 shows the TE reflectivity spectra with WGM resonances with mode orders $n = 1$ to 4 and $l$ numbers as labeled for different applied uniaxial force. The spectra were recorded with the CCD camera in second-order diffraction of the grating spectrometer, yielding a resolution of about

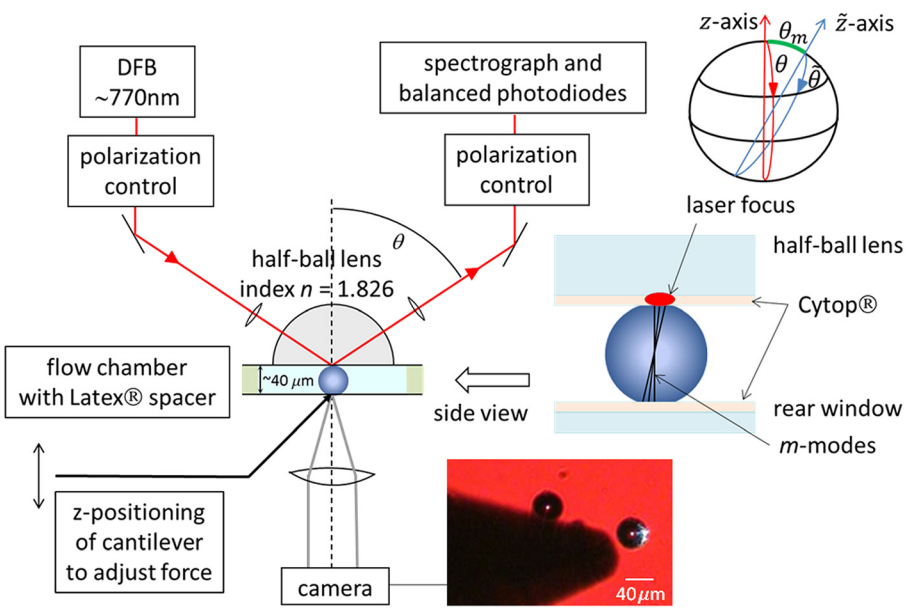


FIG. 1. Sketch of the experimental set-up. On the right a magnified side view of the flow chamber schematically shows the deformed bead with excited $m$-modes in the ray-optical picture. The image at the bottom is taken with a 10× microscope objective through the coverslip and shows two beads and the cantilever close to the excited bead (right).

the $n = 1$–3 modes might be explained by their different coupling with $n \geq 4$ modes. This mode coupling enhances with increasing strain as will be shown in Sec. III B. The observed energy shifts are by a factor of ~50 higher as values reported on solid PMMA microspheres of 460 $\mu$m size[11] which have a comparable modulus of elasticity as polystyrene microspheres.[36] The stress sensitivity of 100 $\mu$N in this polar configuration given by a strain induced shift equal to half of the FWHM of the linewidth is enhanced by a factor of ~10 compared to solid PMMA spheres and is comparable to the sensitivity observed in hollow PMMA beads of 980 $\mu$m size.[11] This finding exemplifies the potential of the polar excitation of small ~50 $\mu$m diameter PMs for pressure sensing.

The energy shifts of the TM WGMs as a function of the applied uniaxial force are shown in Figure 4(b). They are similar to the ones of the TE WGMs shown in Fig. 4(a).

In order to investigate the resonance broadening with increasing uniaxial strain in more detail, we increased the resolution using the scanning DFB laser detection method. Figures 5(a) and 5(b) show photographs of the excited bead in the flow chamber obtained by the camera which is placed behind the thin rear glass window. The exciting laser beam is focused onto the bead from left as shown in Fig. 1. Figure 5(a) shows the bead where the laser wavelength is off resonant while Fig. 5(b) reveals scattering from a two-dimensional surface wave when the laser wavelength is resonant to the WGM.

Normalized high-resolution spectra for the TE $2_{256}$ WGM are given in Figure 6 as a function of the applied force. The center energy of the TE $2_{256}$ WGM mode shifts toward higher energy with a slope of $dE/dF \sim 50\ \mu$eV/mN in agreement with the previous results obtained with the spectrometer. The resonance energies at various uniaxial forces are shown in Fig. 4 as large open symbols. At zero force the FWHM of this mode is $\gamma \sim 8\ \mu$eV which corresponds to a Q factor of $\hbar\omega/\gamma = 2 \times 10^5$. This is by one order of magnitude smaller than values found in free PMs of similar size held by optical tweezers[22,23] and by a factor of 4 larger than observed in solid and hollow PMMA beads.[11] The broadening at zero force in the PM under investigation is therefore attributed to a slight pre-strain causing a splitting of $m$-modes due to the deformed PM at the polar caps. With increasing uniaxial force the linewidth significantly broadens (to ~4 times its FWHM value at zero force), and a splitting into sub-components becomes visible above a force of ~6 mN, which we attribute to WGMs of different $m$-number of the deformed PM (see also magnified side view of the bead in Fig. 1). Further increasing the uniaxial force expands the splitting energy $\Delta_m$ between the different $m$-modes which results in additional broadening of the total WGM linewidth.

In order to determine the average linewidth of the $m$-lines of the TE $2_{256}$ WGM at an applied force of 8.6 mN by a multiple Lorentzian-line fit of split $m$-lines using the function $S_{TE2} = \sum_1^{15} {}^{2A_i}/_{\pi}\left(\frac{\Gamma}{4(x-xc_i)^2+\Gamma^2}\right)$ with areas $A_i$, FWHM $\Gamma$, and center energy positions $xc_i$ being free fitting parameters of 15 Lorentzian-lines. The dashed blue line in Fig. 7 shows the fit, and individual $m$-lines are given as thin black lines. The FWHM linewidth $\Gamma$ of the 15 Lorentzian-lines is $\Gamma = 8 \pm 0.5\ \mu$eV. Similar Lorentzian-line fits of WGM resonances at applied 6.2 and 11.3 mN uniaxial force reveal an average $\Gamma = 5.5 \pm 0.5\ \mu$eV and $11 \pm 0.5\ \mu$eV, respectively, indicating a linear increase of $\Gamma$ with slope $d\Gamma/dF \sim 1.2\ \mu$eV/mN with increasing force as shown in Fig. 8.

experiments the coupling angle and position of the incident DFB laser light has been chosen to predominantly excite the $m=0$ mode (at lowest energy) at zero applied force while the $m=1$ mode is only weakly visible (the small oscillations in the spectra that do not change with applied force are spurious Fabry-Perot interferences). The applied forces on one bead have again been determined using the slope of $dE/dF \sim 40\,\mu$eV/mN of a TE 1 mode obtained from PMs at low offset strain. With increasing applied uniaxial force the intensity of the $m=0$ mode weakens while the $m=1$ mode gains in strength. This can be attributed to changing coupling conditions at the increasingly deformed polar cap. As in the previous experiment with pressurized liquid, the FWHM $\Gamma$ of the $m=0$ mode increases from $\Gamma=11.4\,\mu$eV at zero applied pressure to $\Gamma=16\,\mu$eV at 9.1 mN applied uniaxial force. At forces larger than 11 mN the $m=2$ mode appears on the high energy side of the $m=1$ mode. Above 13 mN the different m-modes merge, resulting in a broad band with a FWHM of $\Gamma \sim 120\,\mu$eV. Figure 11(a) illustrates the obtained energy shift $\Delta E$ of the $m=0$ and $m=1$ resonances as well as of the broad reflection band as function of the applied force. The weakening of the $m=0$ line and the evolution of the $m=1$ mode into a broad $m>1$ band induces a slight nonlinear force dependence of the measured energy shift $\Delta$E of the TE $1_{262}$ WGM.

The measured energy distance $\Delta_m$ between the $m=0$ to $m=1$ line as a function of the applied uniaxial force is displayed in Figure 11(b). The slope has a value of $d\Delta_m/dF \sim 1.1\,\mu$eV/mN which is comparable to the value found for $n=2$ WGM in PMs at low offset strain. With the value $d\Delta_m/dF = 1.1\,\mu$eV/mN the offset uniaxial force of the PM under investigation can be estimated to $F_{\text{offset}} \sim 26$ mN. The value $d\Delta_m/dF$ also allows estimating the force in our experiment where we used liquid pressure to reduce the force on the PM. The calculated uniaxial force values range from $F=12$ mN to 26 mN as labeled in Fig. 9. The inset in Fig. 11(b) shows the FWHM $\Gamma$ of the $m$-modes as a function of the total uniaxial force on the bead obtained from Figs. 9 and 10. It suggests a linear increase of the line broadening $\Gamma$ with a slope of $d\Gamma/dF = 0.47\,\mu$eV/mN with increasing uniaxial strain. The linewidth increase is attributed to increasing scattering losses at the deformed polar caps of the bead.

Figure 12 displays the TE/TM reflectivity ratio as in Figure 2 of WGM resonances of a highly pre-strained PM as a function of applied uniaxial force. The spectra were recorded with the CCD camera using the high-resolution grating spectrometer. The coupling conditions in this experiment were chosen to support the excitation of the $n=1$ to 3 mode while the broad $n=4$ mode is only weakly excited. Like for the other mode orders $n$, the mode numbers $l$ (given as subscript) and the sphere size have been determined by comparing the resonance energies with calculations. High resolution spectra of the TE $1_{262}$ WGM using the scanning DFB laser show a splitting energy between $m$-modes of $\Delta_m \sim 46\,\mu$eV (not shown here). The splitting suggests an offset

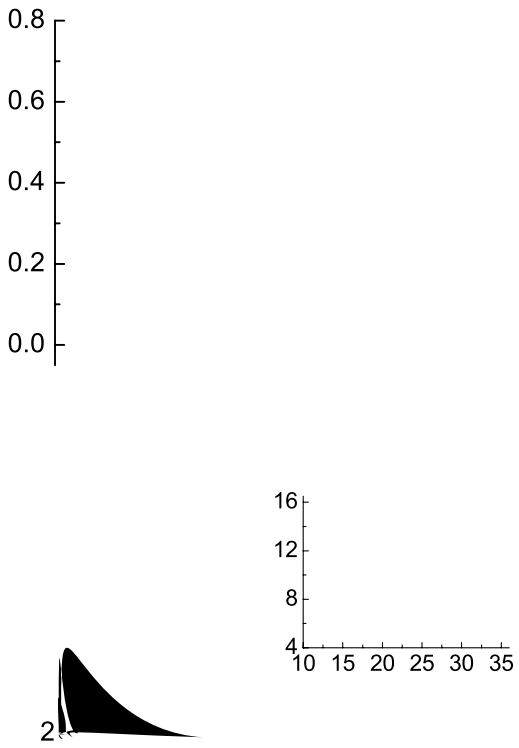

force of $F_{\text{offset}} \sim 42$ mN where the slope value of the $m$-splitting of 1.1 $\mu$eV/mN derived from the previous PM is used. Again, the applied force on one bead has been determined using the slope of $dE/dF \sim 50$ $\mu$eV/mN (compare Fig. 4) for the TE 2 mode at low applied uniaxial force (near $F_{\text{offset}}$). The measurements demonstrate that with increasing applied uniaxial force the WGMs TE $1_{264}$ and TE $2_{257}$ approach each other and that this approach leads to a weakening of the TE $1_{264}$ and strengthening of the TE $2_{257}$ in the signal. A similar behavior is found between the WGMs TM $2_{255}$ and TM $3_{247}$. As discussed earlier, the modes significantly broaden with increasing uniaxial force.

Figure 12 (bottom) summarizes the resulting shifts of the TE and TM WGM resonance energies $E$ with mode orders $n = 1$ to 4 as a function of the uniaxial force. The shifts reveal a super-linear force dependence. Using a low-force linear slope of $dE/dF \sim 50$ $\mu$eV/mN for the TE $2_{257}$ mode an initial slope of $dE/dF \sim 40$ $\mu$eV/mN for the TM $3_{247}$ is deduced from the data which is in agreement with the value found for beads at low offset stress. The WGM TE $1_{264}$ and TM $2_{255}$ show a higher slope of $dE/dF \sim 60$ $\mu$eV/mN, which is predominantly attributed to their approach to the WGMs TE $2_{257}$ and TM $3_{247}$, respectively. The TE and TM $n = 4$ modes have the highest slope of $dE/dF \sim 200$ $\mu$eV/mN, about 3 times higher as compared to investigations on weakly pre-strained PMs. However, at high force the $n = 1$ to 3 modes also reach similar slope values possibly indicating an increasing mixing between the $n = 1$ to 4 modes.

## IV. THEORETICAL MODELING

### A. Energy shift of the WGM modes under uniaxial strain

In the ray optics model a resonance occurs when the light wave interferes constructively with itself after one roundtrip along the inner surface of the bead. In this model the resonance condition is given approximately by

$$C n_0 = 2\pi a\, n_0 = l\lambda, \tag{1}$$

where $l$ is the number of wavelengths in the optical path of one roundtrip, the circumference $C$ is expressed by the radius of the bead $a$, and the refractive index of the bead $n_0$. In this ray picture, the path of the light inside the bead follows polygons with $s$-sides, where $s$ is the number of total internal reflections at the inner surface. The smaller the number of reflections $s$, the larger is the radial component of the wave vector increasing the number of radial nodes. Thus, the radial mode order $n$ is increasing with the ray length between successive reflections. Uniaxial pressure that is exerted on the bead will create flat caps at the poles. Thus, the centrifugal term in the wave equation is missing at the poles.[1,2] Accordingly, the waves reflecting from the poles cut longer chords into the bead instead of being guided along its inner surface which could cause a mixing with higher order $n$-modes. On the other hand the compression at the poles increases the refractive index locally. Therefore, the poles act as graded index lenses (GRIN) which guide the modes along the flat caps and thus compensate the effect of the missing centrifugal potential. We therefore make the assumption that the resonating modes are still guided closely underneath the surface, and we describe the shift $\Delta\lambda$ in the resonance wavelength $\lambda$ as a change in the optical path by

$$\begin{aligned}\frac{\Delta\lambda}{\lambda} &= \frac{dC(F)}{C} + \frac{dn_0(F)}{n_0} \\ &= \frac{1}{2\pi}\int_0^{2\pi}\left(\frac{\sqrt{(a+u_r(F,\theta))^2 + u_\theta(F,\theta)^2} - a}{a} + \frac{dn_0(F,\theta)}{n_0}\right)d\theta,\end{aligned} \tag{2}$$

where $u_r(F,\theta)$ and $u_\theta(F,\theta)$ are the radial and azimuthal component of the static displacement vector $\vec{u}$, which describes the displacement that a point at $\vec{r}$ within the isotropic solid of the PM experiences under the external force. The displacement $\vec{u}$ respects the Navier equation[38,39]

$$\nabla^2\vec{u} + \frac{1}{1-2\nu}\nabla(\nabla\cdot\vec{u}) = 0, \tag{3}$$

where $\nu$ is the Poisson ratio. In spherical coordinates, the solution of this differential equation under axisymmetrical and torsionless load can be expressed[39] by the radial and azimuthal components

$$\begin{aligned}u_r &= \sum_n \{A_n(n+1)(n-2+4\nu)r^{n+1} + B_n n r^{n-1}\}P_n(\cos\theta), \\ u_\theta &= \sum_n \{A_n(n+5-4\nu)r^{n+1} + B_n r^{n-1}\}\frac{d}{d\theta}P_n(\cos\theta), \\ u_\varphi &= 0.\end{aligned} \tag{4}$$

The displacement is described as a superposition of static surface waves on the sphere. The coefficients $A_n$ and $B_n$ depend on the actual pressure on the sphere. For a uniaxial pressure in z-direction,[40,41] the radial pressure component

$$p(\theta) = \frac{3F}{2\pi a_0^3}\sqrt{a_0^2 - a^2\sin^2(\theta)} \tag{5}$$

is exerted on the sphere by non-deformable plates and flat caps are formed at the poles of the PM. In Eq. (5), $F$ and $a = 22.5$ $\mu$m are the force and the radius of the sphere, respectively. The radius $a_0(F)$ of the contact area at the poles can be found using Hertz' pressure formula[40,41]

$$a_0(F) = \left(\frac{3Fa\,(1-\nu^2)}{4E}\right)^{1/3}, \tag{6}$$

where in our case the Poisson ratio for polystyrene is $\nu = 0.325$ (Ref. 36) and the modulus of elasticity is $E = 3.3$ GPa.[36] Because the unperturbed geometry is spherical, it is appropriate to expand the pressure $p(\theta)$ in terms of spherical harmonics, i.e., Legendre polynomials

$$p(\theta) = \sum_n H_n P_n(\cos(\theta)). \tag{7}$$

The expansion coefficients $H_n$ can be found using the orthogonality of the Legendre polynomials $P_n$, yielding

$$H_n = \frac{2n+1}{2}\int_0^{\pi} P_n(\cos\theta)\, p(\theta)\sin\theta\, d\theta. \tag{8}$$

Since the pressure is applied symmetrically from both poles, the system has the symmetry $\theta \leftrightarrow \pi - \theta$ and the coefficients for Legendre polynomials for odd integers $n$ are zero. For even $n$, $A_n$ and $B_n$ in Eq. (4) are given by[39]

$$\begin{aligned} A_n &= -\frac{H_n}{4Ga^n\{n+2n\nu+1+\nu+n^2\}}, \\ B_n &= \frac{H_n\,(n^2+2n-1+2\nu)\,a^{2-n}}{4G\,\{2n^2\nu-n\nu+n^3-1-\nu\}}. \end{aligned} \tag{9}$$

In Eqs. (8) and (9) $G$ is the shear modulus which is equal to $G = (E/2)(\nu+1)^{-1}$. Fig. 13 shows the radial displacement $u_r$ for four different forces, $F = 5$, 10, 40, and 50 mN where the series of Legendre polynomials has been truncated at $n = 60$. In all cases the calculated displacement $u_r$ at $\theta = 0$ is close to the displacement at the pole of an infinite half sphere given as $h = a_0^2/a$.[40,41] Fig.13 also shows the calculated azimuthal displacement $u_\theta$ for a force of 50 mN (dashed blue line). Since $u_\theta^2$ is small compared to $(a+u_r)^2$ we neglect $u_\theta$ in Eq. (2) which simplifies the first term to $\frac{dC}{C} = \frac{1}{2\pi}\int_0^{2\pi}\frac{u_r(F,\theta)}{a}d\theta$. Shown in insets (a) and (b) are parts of the deformed sphere with radius $a + u_r(F,\theta)$ (dashed blue line) at the pole and at the equator, respectively, at a uniaxial force of $F = 50$ mN. The undeformed sphere is shown as a solid line for comparison.

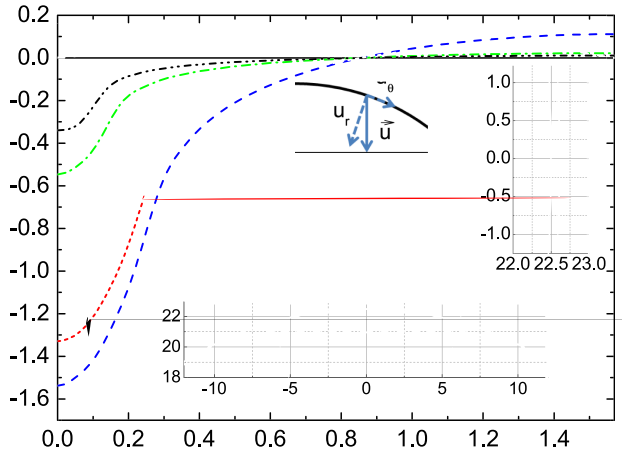


The change in refractive index $dn_0$ is determined by the stress inside the sphere caused by the pressure (Eq. (5)), which leads to compression inside the flat cap in all three dimensions.[40] The principal stresses $\sigma_x$, $\sigma_y$, and $\sigma_z$ within the contact area ($\theta < \theta_0$) are given by[42]

$$\begin{aligned} \sigma_x(F) &= p_0\left(2\nu\sqrt{1-\frac{(a\sin\theta)^2}{a_0(F)^2}} + \frac{1-2\nu}{3}\frac{a_0(F)^2}{(a\sin\theta)^2}\left[1-\left(1-\frac{(a\sin\theta)^2}{a_0(F)^2}\right)^{3/2}\right]\right), \\ \sigma_y(F) &= p_0\left(\sqrt{1-\frac{(a\sin\theta)^2}{a_0(F)^2}} - \frac{1-2\nu}{3}\frac{a_0(F)^2}{(a\sin\theta)^2}\left[1-\left(1-\frac{(a\sin\theta)^2}{a_0(F)^2}\right)^{3/2}\right]\right), \\ \sigma_z(F) &= p_0\sqrt{1-\frac{(a\sin\theta)^2}{a_0(F)^2}}, \end{aligned} \tag{10}$$

where $\theta_0 = \arcsin(a_0/a)$ and $p_0$ is the central pressure at the pole. Outside the contact area $\sigma_z$ vanishes. The two remaining principal stresses are the compression $\sigma_x$ and the tension $\sigma_y$ which compensate each other

$$\begin{aligned} \sigma_x(F) &= p_0\frac{1-2\nu}{3}\frac{a_0(F)^2}{(a\sin\theta)^2}, \\ \sigma_y(F) &= -p_0\frac{1-2\nu}{3}\frac{a_0(F)^2}{(a\sin\theta)^2}. \end{aligned} \tag{11}$$

The principal stresses are connected with the local change of the refractive index $dn_0(F)$ by the optoelastic constants $K_1$ and $K_2$ which have values ranging from 0.50 to $0.65\times10^{-10}\mathrm{Pa}^{-1}$ (Refs. 36, 43, and 44) (the optoelastic constants $K_1$ and $K_2$ have been derived from the elasto-optical coefficients $p_{11}$ and $p_{22}$). Since our experiments did not show significantly different shifts for TE and TM modes (see Fig. 4) we neglect birefringence and set $K = (K_1+K_2)/2$. Accordingly, the refractive index change $dn_0(F)$ is given by

$$dn_0(F) = K\left(\sigma_x(F)+\sigma_y(F)+\sigma_z(F)\right). \tag{12}$$

The sum of the calculated stresses $\sigma_x+\sigma_y+\sigma_z$ at the surface for applied uniaxial forces of 5, 10, 40, and 50 mN is shown in Figure 14. The inset shows the refractive index $n_0 + dn_0(F)$ (dashed blue line, with $n_0 = 1.58$) of the deformed PM at an applied force of 50 mN in a polar coordinate plot using a value of $K = 0.57\cdot10^{-10}\,\mathrm{Pa}^{-1}$.

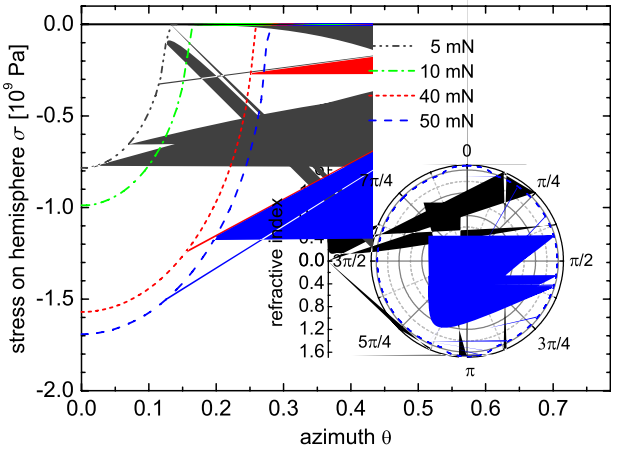


FIG. 14. Total stress on the surface of the hemisphere as a function of the azimuth $\theta$ for uniaxial forces 5, 10, 40, and 50 mN, as labeled. The inset shows the resulting refractive index (dashed blue line) at the deformed polar caps in a polar plot at an applied uniaxial force of 50 mN.

The shift of the WGM resonance due to the change in refractive index according to the second term in Eq. (2) is given by

$$\frac{1}{2\pi}\int_0^{2\pi}\frac{dn_0(F)}{n_0}d\theta=\frac{2K}{\pi n_0}\left(\int_0^{\pi/2}\left(\sigma_x(F)+\sigma_y(F)+\sigma_z(F)\right)d\theta\right). \tag{13}$$

The changes of the geometric path as well as the change of the refractive index (Eq. (13)) are plotted in Fig. 15. The compression induced increase of the refractive index (see dashed-dotted curve) is shifting the modes to longer wavelengths. This increase of the refractive index is nearly proportional to $F^{2/3}$. The compression induced change of the geometrical path (dashed curve) is shifting the modes to shorter wavelengths, overcompensating the refractive index effect. Its dependence on the force $F$ is more complicated but can be approximated by a function of the form $F^x$ with $x=0.84$. The measured differential shifts obtained from our experiments (data points) are in reasonable agreement with the theoretical curve (solid line) for uniaxial forces larger than 5 mN, which indicates a differential shift of approximately 75 $\mu$eV/mN (the data points for the modes $n=1$, 2, and 3 were derived from Figs. 4, 11 and 12 by dividing the energy shift of each mode by the extrapolated initial energy). The weaker increase of the refractive index change compared to the geometric path change at higher uniaxial stresses ($F>40$ mN) further explains the experimentally observed nonlinear behavior of the differential shift at higher applied forces (see Fig. 12). For small forces (<10 mN) our model overestimates the refractive index change caused by the applied stress. We attribute this deviation mainly to the finite stiffness of the thin rear window and of the Cytop® layer. The Cytop® layer is likely to deform under the pressure by the PM which reduces the total stress within the contact area more as the circumference of the deformed PM bead.

Our theoretical model does not predict that the strain induced shift of the spectrally broad $n=4$ mode is stronger nor that it should show a nonlinear behavior with force coefficients increasing from 70 up to 200 $\mu$eV/mN with increasing uniaxial strain. The larger strain-induced shift of the $n=4$ mode might be caused by its coupling to the substrate.[35] It might also be necessary to take into account that the wave functions of the $n$-modes differ in their radial expectation values and thus experience different spatial stresses and refractive indices inside the PM. Treating these details requires a solution of the wave equation taking in the three-dimensional refractive index distribution created by the strain, which is beyond the scope of this work.

### B. M-mode splitting under uniaxial strain

In order to describe the effect on different $m$-modes we modified the integral in Eq. (2) into an integral that follows a great circle $\tilde{\theta}=0...\pi/2$ inclined by the angle

$$\theta_m=\frac{\pi}{2}-\arccos\frac{m}{\sqrt{l(l+1)}}, \tag{14}$$

with respect to the z-axis of the untilted system, resulting in an integral over $\tilde{\theta}$

$$\left(\frac{\Delta\lambda(F)}{\lambda}\right)=\frac{2}{\pi}\int_0^{\pi/2}\frac{u_r(F,\theta(\tilde{\theta},\theta_m))}{a}+\frac{dn_0(F,\theta(\tilde{\theta},\theta_m)}{n_0}d\tilde{\theta}. \tag{15}$$

The integrands, however, still depend on the angle $\theta$ of the untilted system. $\theta$ and $\tilde{\theta}$ have the same latitude in the untilted system (Fig. 1) and are connected by $\theta(\tilde{\theta},\theta_m)=\arccos(\cos\tilde{\theta}\cos\theta_m)$. The resulting shifts for $F=10$ mN and 40 mN are presented in Fig. 16. The mode number $l$ was set to $l=265$. The effect of the compression induced increase of the refractive index (dashed-dotted curve, $F=10$ mN) extends over a narrower angular range than the effect of the reduction of the effective radius of the PM (long dashed curve, $F=10$ mN). This leads for small pressures to

0 10 20 30 40

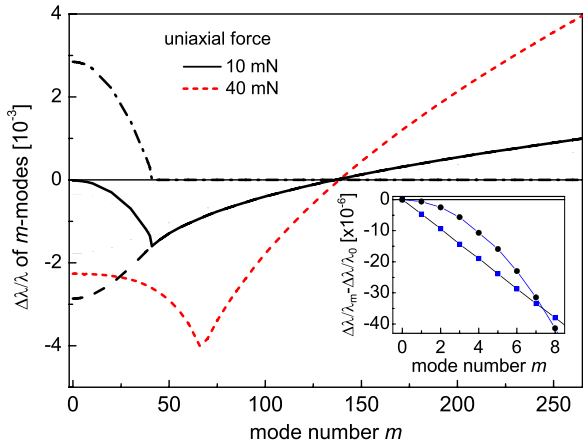


FIG. 16. Relative wavelength shifts due to the change of the refractive index $n$ (dashed-dotted line), the change in circumference $C$ (long dashed line), and the total differential shift (solid line) for different $m$-modes at a uniaxial force of $F = 10$ mN. The total differential shift for $F = 40$ mN is represented by the short-dashed line. The inset shows the differential shift of the first eight $m$-modes relative to the $m = 0$ mode. For comparison the experimental differential shifts are added (blue squares) using an energy splitting $\Delta_m$ of 7.5 $\mu$eV obtained from Fig. 8.

a blue shift that increases with $m$ (solid line), which agrees with the experimental findings (see Fig. 9). The effect reverses for modes outside the contact area of the cap. At $F = 10$ mN, this would be the case for modes $m > 40$ or around $\sim 9^\circ$. Since we observe only modes up to $m = 15$, we were not able to verify this prediction. The PM bulges outward around the equator, resulting in a redshift for modes with $\theta_m \geq 34^\circ$ ($m > 150$). The equatorial mode $m = l$ is the mode with the largest red shift and has been extensively studied by various groups.[11–13,45] In contrast to the results of our experiments (compare to Fig. 8) the calculated energy splitting between the first successive $m$-modes (between $m$ and $m+1$) is not equal, but has a nearly quadratic dependence for modes $m < 5$ as demonstrated in the insert of Fig. 16. At $F = 10$ mN, the average $m$-splitting is the same as the measured one in Fig. 8, namely, $\Delta_m \approx 7.5$ $\mu$eV. The discrepancy between the curves might be related to the form of the contact between the PM and the Cytop®. As mentioned before the Cytop® layer is likely to deform by the PM, and thus the analytical strain distribution at the interface could be different.

Generally, we find that the ray optics approach can explain most of the experimentally observed features, despite its approximations compared to the full wave-optics treatment. The remaining deviations, like the nearly quadratic versus the linear dependence of the $m$-splitting and the fact that the splitting between the $m$-modes increases with increasing force, might be related to this approximation, which treats the WGMs as quantized classical paths, a relatively simple approximation of their two-dimensional surface wave character that is visible in Fig. 5. A full wave model of the system and an accurate knowledge of the contact geometry are needed to describe these properties in more detail.

## V. SUMMARY AND CONCLUSIONS

We have investigated the effects of uniaxial stress on polar TE and TM WGMs in solid PM of $\sim 43$ $\mu$m size using reflection measurements. In our experiments the applied uniaxial force on the PM ranges from nearly 0 to $\sim 70$ mN. The resonating $n$-modes reveal a blue shift due to the decrease of the geometrical circumference of the deformed microsphere. The pressure on the polar caps locally increases the refractive index which partially compensates the effect of the smaller circumference, resulting in a strain induced, almost linear energy shift with a force coefficient of $dE/dF \sim 40$ $\mu$eV/mN for $n = 1$ and 3 and of $\sim 50$ $\mu$eV/mN for $n = 2$ modes for uniaxial forces up to 45 mN. The shifts of TE and TM modes were similar, indicating an insignificant influence of birefringence. In addition, the WGMs broaden with increasing applied force which is attributed to larger losses at the edges of the flat caps. We also observe a strain-induced splitting of the WGMs, which is described for small $m \ll l$ by an additional shift proportional to $m$ with a coefficient of about 1 $\mu$eV/mN. The linewidths of the $m$-modes increase proportional to $m$ and proportional to the uniaxial strain, which is also attributed to increased scattering losses at the deformed polar caps. For uniaxial forces exceeding $\sim 45$ mN the strain induced blueshift of the $n = 1$ to 3 WGMs increases nonlinearly and approaches the force coefficient and linewidth of the $n = 4$ WGM. This behavior is probably due to mixing between the $n = 1$ to 4 modes at high force levels.

The experimental results have been compared with a theoretical model which is based on quantized ray-optics. This approach predicts a blue-shift of the WGMs that is almost linearly increasing for applied forces larger than 10 mN. The theoretically obtained coefficient of $\sim 75$ $\mu$eV/mN is higher but in the same order of magnitude as the experimentally observed value for the $n = 1$ to 3 WGM modes. Deviations of the model calculations with the experimental values are attributed to our assumption that the Cytop® layers and windows are rigid. Our model further explains the splitting of the $m$ - modes as a function of applied uniaxial pressure. The calculations confirm that higher order $m$- modes have a larger blue shift compared to lower order $m$-modes since the pressure induced increase of the refractive index (causing an energy red-shift) extends over a narrower angular range than the decrease of the geometrical path. While the calculated strain-induced $m$-splitting coefficients $d\Delta_m/dF$ are in the same order of magnitude as the measurements, the predicted quadratic increase of $d\Delta_m$ with increasing $m$-number is in contrast to the experimental data which show a linear increase. This deviation could be related to the deformation of the Cytop® layer that is not accounted for in the model. Generally, we expect that the quantized ray-optic approach will create inaccuracies compared to the full wave model, which will be subject of further investigations.

## ACKNOWLEDGMENTS

This work has been supported by the Research Corporation for Science Advancement under Grant No. CC6339, by the Biotechnology and Biological Sciences Research Council under Grant No. BB/E005624, and by the Engineering and Physical Sciences Research Council under Grant No. EP/F006683. P.B. acknowledges the Engineering

and Physical Sciences Research Council for her Leadership fellowship award Grant No. EP/I005072/1. Bernd Rossa and Marco Fatuzzo are acknowledged for valuable discussions regarding the theoretical modeling.

[1]A. B. Matsko and V. S. Ilchenko, IEEE J. Sel. Top. Quantum Electron. **12**, 3 (2006).
[2]V. S. Ilchenko and A. B. Matsko, IEEE J. Sel. Top. Quantum Electron. **12**, 15 (2006).
[3]I. S. Grudinin, A. B. Matsko, A. A. Savchenkov, D. Strekalov, V. S. Ilchenko, and L. Maleki, Opt. Commun. **265**, 33 (2006).
[4]V. S. Ilchenko, A. A. Savchenkov, J. Byrd, I. Solomatine, A. B. Matsko, D. Seidel, and L. Maleki, Opt. Lett. **33**, 1569 (2008).
[5]M. Cai, O. Painter, K. J. Vahala, and P. C. Sercel, Opt. Lett. **25**, 1430 (2000).
[6]W. Liang, V. S. Ilchenko, A. A. Savchenkov, A. B. Matsko, D. Seidel, and L. Maleki, Opt. Lett. **35**, 2822 (2010).
[7]S. Chang, R. K. Chang, A. D. Stone, and J. U. Noeckel, J. Opt. Soc. Am. B **17**, 1828 (2000).
[8]H. Yukawa, S. Arnold, and K. Miyano, Phys. Rev. A **60**, 2491 (1999).
[9]H. C. Tapalian, J. P. Laine, and P. A. Lane, IEEE Photon. Technol. Lett. **14**, 1118 (2002).
[10]Q. Ma, T. Rossmann, and Z. Guo, Meas. Sci. Technol. **21**, 025310 (2010).
[11]T. Ioppolo, M. I. Kozhevnikov, V. Stepaniuk, M. V. Otugen, and V. Sheverev, Appl. Opti. **47**, 3009 (2008).
[12]T. Ioppolo, U. K. Ayaz, and M. V. Otugen, J. Appl. Phys. **105**, 013535 (2009).
[13]V. S. Ilchenko, P. S. Volikov, V. L. Velichansky, F. Treussart, V. Lefevre-Seguin, J. M. Raimond, and S. Haroche, Opt. Commun. **145**, 86 (1998).
[14]M. Manzo, T. Ioppolo, U. K. Ayaz, V. LaPenna, and M. V. Oetuegen, Rev. Sci. Instrum. **83**, 105003 (2012).
[15]A. A. Savchenkov, V. S. Ilchenko, W. Liang, D. Eliyahu, A. B. Matsko, D. Seidel, and L. Maleki, Opt. Lett. **35**, 1572 (2010).
[16]T. Ioppolo, U. Ayaz, and M. V. Otugen, Opt. Express **17**, 16465 (2009).
[17]T. Ioppolo, J. Stubblefield, and M. V. Oetuegen, J. Appl. Phys. **112**, 044906 (2012).
[18]T. Ioppolo, M. V. Otugen, and K. Marcis, J. Appl. Phys. **107**, 123115 (2010).
[19]T. Ioppolo, V. Otugen, D. Fourguette, and L. Larocque, J. Opt. Soc. Am. B: Opt. Phys. **28**, 225 (2011).
[20]M. S. Luchansky and R. C. Bailey, Anal. Chem. **84**, 793 (2012).
[21]A. B. Matsko, A. A. Savchenkov, V. S. Ilchenko, D. Seidel, and L. Maleki, J. Lightwave Technol. **28**, 3427 (2010).
[22]J. Lutti, W. Langbein, and P. Borri, Appl. Phys. Lett. **91**, 141116 (2007).
[23]J. Lutti, W. Langbein, and P. Borri, Appl. Phys. Lett. **93**, 151103 (2008).
[24]T. Ioppolo, N. Das, and M. V. Otugen, J. Appl. Phys. **107**, 103105 (2010).
[25]V. R. Dantham, S. Holler, V. Kolchenko, Z. Wan, and S. Arnold, Appl. Phys. Lett. **101**, 043704 (2012).
[26]M. Baaske and F. Vollmer, ChemPhysChem **13**, 427 (2012).
[27]X. Lopez-Yglesias, J. M. Gamba, and R. C. Flagan, J. Appl. Phys. **111**, 084701 (2012).
[28]C. C. Lam, P. T. Leung, and K. Young, J. Opt. Soc. Am. B **9**, 1585 (1992).
[29]Q. Song, L. Ge, B. Redding, and H. Cao, Phys. Rev. Lett. **108**, 243902 (2012).
[30]A. Mekis, J. U. Nockel, G. Chen, A. D. Stone, and R. K. Chang, Phys. Rev. Lett. **75**, 2682 (1995).
[31]Q. H. Song, L. Ge, A. D. Stone, H. Cao, J. Wiersig, J. B. Shim, J. Unterhinninghofen, W. Fang, and G. S. Solomon, Phys. Rev. Lett. **105**, 103902 (2010).
[32]B. Redding, L. Ge, G. S. Solomon, and H. Cao, Appl. Phys. Lett. **100**, 061125 (2012).
[33]Y.-F. Xiao, C.-H. Dong, Z.-F. Han, G.-C. Guo, and Y.-S. Park, Opt. Lett. **32**, 644 (2007).
[34]H. G. L. Schwefel, N. B. Rex, H. E. Tureci, R. K. Chang, A. D. Stone, T. Ben-Messaoud, and J. Zyss, J. Opt. Soc. Am. B: Opt. Phys. **21**, 923 (2004).
[35]L. Chantada, N. I. Nikolaev, A. L. Ivanov, P. Borri, and W. Langbein, J. Opt. Soc. Am. B: Opt. Phys. **25**, 1312 (2008).
[36]P. Zhengcai, "The opto-elastic constant has been derived from the thermal expansion coefficient and the constant dn/dT," in *Polymer Data Handbook*, edited by J. E. Mark (Oxford University Press, New York, 1999), pp. 829–836.
[37]T. Ioppolo and M. V. Oetuegen, J. Opt. Soc. Am. B: Opt. Phys. **24**, 2721 (2007).
[38]A. E. H. Love, *Treatise on the Mathematical Theory of Elasticity*, 4th ed. (Cambridge University Press, 1952).
[39]R. W. Soutas-Little, *Elasticity* (Dover, Mineola, New York, 1999), pp. 315–400.
[40]H. Hertz, J. Reine Angew. Math. **92**, 156 (1881).
[41]L. D. Landau and E. M. Lifshitz, *Theory of Elasticity*, 2nd ed. (Pergamon Press, New York, 1959), pp. 30–37.
[42]M. T. Huber, Ann. Phys. **14**, 103 (1904).
[43]T. M. Smith and A. Korpel, IEEE J. Quantum Electron. **1**, 283 (1965).
[44]K. Vedam, J. A. Meyers, and G. R. Mariner, J. Appl. Phys. **47**, 2443 (1976).
[45]H. M. Lai, P. T. Leung, K. Young, P. W. Barber, and S. C. Hill, Phys. Rev. A **41**, 5187 (1990).